

1 Calcium modeling of spine apparatus containing 2 human dendritic spines demonstrates all-or-nothing 3 communication switch between the spine head and 4 dendrite

5 James Rosado^{1,*}, Viet Duc Bui^{2,*}, Carola Haas^{3,4,5,6}, Jürgen Beck^{3,6}, Gillian Queisser^{1,2,\$,§},
6 and Andreas Vlachos^{2,4,5,6,\$,§}

7 ¹Department of Mathematics, Temple University, Philadelphia, USA

8 ²Department of Neuroanatomy, Institute of Anatomy and Cell Biology, Faculty of Medicine, University of Freiburg,
9 Freiburg, Germany

10 ³Department of Neurosurgery, Medical Center-University of Freiburg, Faculty of Medicine, University of Freiburg,
11 Freiburg, Germany

12 ⁴Bernstein Center Freiburg, University of Freiburg, Freiburg, Germany

13 ⁵Center Brain Links Brain Tools, University of Freiburg, Freiburg, Germany

14 ⁶Center for Basics in NeuroModulation (NeuroModulBasics), Faculty of Medicine, University of Freiburg, Freiburg,
15 Germany

16*these authors contributed equally to this work

17§Joint senior authors

18§Correspondence to gillian.queisser@temple.edu and andreas.vlachos@anat.uni-freiburg.de

19 ABSTRACT

20 Example Abstract. Abstract must not include subheadings or citations. Example Abstract. Abstract must not include
subheadings or citations. Example Abstract. Abstract must not include subheadings or citations. Example Abstract. Abstract
must not include subheadings or citations. Example Abstract. Abstract must not include subheadings or citations. Example
Abstract. Abstract must not include subheadings or citations. Example Abstract. Abstract must not include subheadings or
citations. Example Abstract. Abstract must not include subheadings or citations.

21 Please note: Abbreviations should be introduced at the first mention in the main text – no abbreviations lists. Suggested
22 structure of main text (not enforced) is provided below.

23 Introduction

24 Calcium-based second-messenger signaling pathways mediate fundamental biological processes in the human body (Berridge
25 et al., 2000). In the brain, synaptically evoked intracellular Ca²⁺ surges regulate the ability of neurons to adjust their synaptic
26 contacts in an activity-dependent manner (Holthoff et al., 2006; Higley et al., 2008). This fundamental biological mechanism,
27 i.e., synaptic plasticity, plays a crucial role in complex brain functions, such as memory formation and learning (Sala and Segal,
28 2014; Padamsey et al., 2019). Over the past few decades, cellular and molecular mechanisms of Ca²⁺ dependent synaptic
29 plasticity have been extensively studied in dendritic spines across various animal models (Higley et al., 2012; Maggio and
30 Vlachos, 2014). Dendritic spines are highly dynamic neuronal compartments on which cortical excitatory synapses are typically
31 formed (Yuste et al., 1995; XXX). The majority of spines have a bulbous head and a thin neck that connects the spine head to
32 the shaft of the dendrite. They often harbor a dynamic extension of the smooth endoplasmic reticulum (sER) in the dendrite,
33 that can rapidly enter and leave the spine compartment and changes its position inside the neck and head of spines (XXX;
34 Perez-Alvarez et al., 2020). Indeed, a critical role for sER intracellular Ca²⁺ stores in synaptic plasticity has been demonstrated
35 (Verkhratsky, 2005; Vlachos et al., 2009; Kokortian et al., 2014). The variable nature of spine morphology and intracellular
36 Ca²⁺ stores has been studied with respect to electrical and biochemical signaling (Tønnesen and Nägerl, 2016; Nishiyama and
37 Yasuda, 2015; Cartailler et al., 2018; ...). In recent work, the influence of synaptic spine architecture on calcium signaling
38 was studied by parametrically designing the leading features of spines, i.e. spine neck width/length, spine head volume, and
39 the size of the sER and performing computational studies on a vast array of synthetically designed geometries (Bell et al.,

40 2019; Basnayake et al., 2019; Breit et al., 2018). Guided by the existing body of literature and our own previous work (REFs;
 41 Breit et al., 2018; Lenz et al., 2021), we decided to carry out a detailed anatomical reconstruction of human cortical spines
 42 based on serial transmission electron microscopy and performing a correlation analysis on a set of geometric features, such as
 43 the size and position of the postsynaptic density, spine head volumes, and cross-sectional areas of spine neck (Figure 1). We
 44 then posed the question how the distinct three-dimensional ultrastructural organization of human dendritic spines influences
 45 intracellular Ca²⁺ dynamics in the spine head and neck, and how these signals propagate into the attached dendritic shaft, i.e.,
 46 spine-to-dendrite Ca²⁺ communication. Specifically, we were interested in learning more about the role of the spine apparatus
 47 organelle (SA; Gray 1959; Spacek 1985; Spacek & Harris 1997), an enigmatic cellular organelle composed of stacked sER,
 48 found in the majority of human cortical dendritic spines (Lenz et. al. 2021).

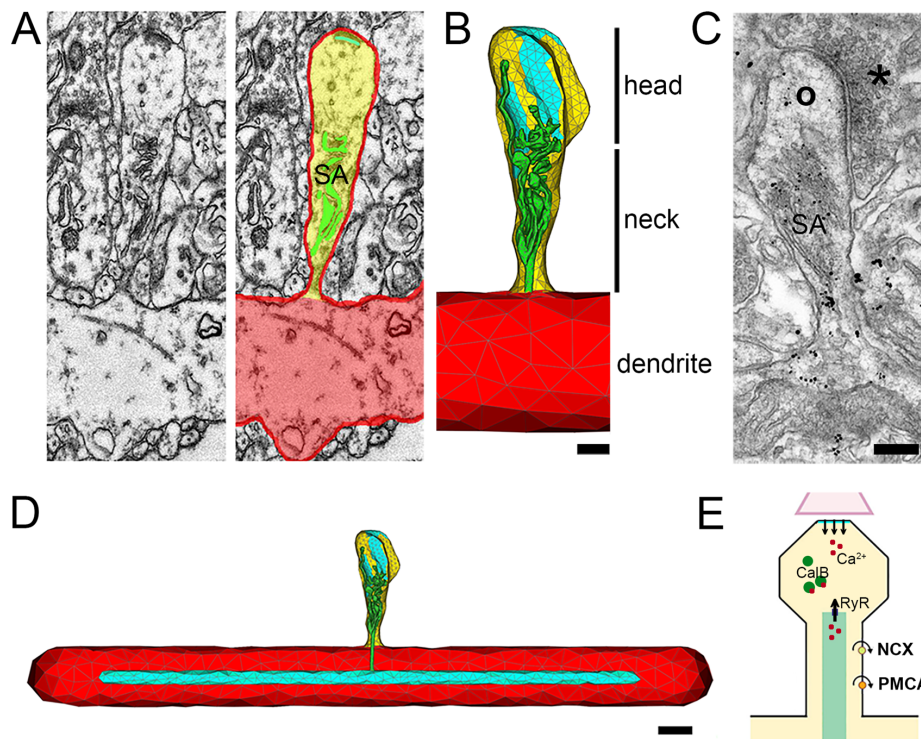


Figure 1. Dendritic spine reconstruction and Ca²⁺ modeling. (A) Spine morphologies are based on serial reconstructions of transmission electron micrographs obtained from human cortical tissue. (B) An example of a reconstructed dendritic spine (dendrite, red; spine compartment, yellow) carrying a spine apparatus organelle (SA, green). Upon release of Ca²⁺ at the reconstructed postsynaptic density (cyan), changes in [Ca²⁺] are determined in the head, neck and dendritic region, respectively. Scale bar, 200 nm. (C) Immunogold staining for the actin-binding protein synaptopodin, which is a marker and essential component of the SA. Asterisk indicates presynaptic, circle the postsynaptic compartment. Scale bar, 200 nm. (D) In all reconstructed human spines the SA was attached to a single standardized dendritic ER tubule in a dendritic compartment with identical dimensions. Scale bar, 500 nm. (E) The model accounts for Ca²⁺ exchange mechanisms on the plasma membrane (Na⁺/Ca²⁺ exchangers (NCX), plasma membrane Ca²⁺ ATPases (PMCA)) and on the ER (green; ryanodine-receptors (RyR)). Calcium buffering capacity (Calbindin, CalB) is kept constant. Further details are provided in the main text and in Tables xxx. See also supplemental movie.

49 Results

50 Spine Ca²⁺ modeling in reconstructed human dendritic spines containing a spine apparatus organelle

51 To capture the effect of the SA on Ca²⁺ dynamics in dendritic spines, the three-dimensional architecture of dendritic spines,
 52 including intracellular membrane structures, must be carefully considered. Extending on the results obtained from synthetically
 53 generated dendritic spines (Breit et al. 2018) the detailed morphologies of 9 dendritic spines, their SA and postsynaptic densities
 54 (PSD) were reconstructed from cortical surgical access material using serial transmission electron microscopy (TEM). From
 55 serial TEM image stacks realistic three-dimensional geometric models were generated (Figure 1A, B).

56 Immunogold staining for the actin-binding protein synaptopodin, which is an essential component for the formation of
 57 the SA in the rodent brain (Deller et al., 2003; Vlachos et al., 2013), confirmed that synaptopodin is a marker for the human

SA (Figure 1C; c.f., Lenz et al., 2020). The reconstructed SAs were then attached to a single standardized dendritic ER tubule in a dendritic compartment of identical dimensions for all spines (Figure 1D). The resulting surface triangulation of the plasma membrane, the SA, the PSD, and dendritic ER were then used to construct a volumetric tetrahedral mesh for numerical simulations.

Existing single-channel models of Ca²⁺ exchangers in the plasma membrane, i.e., plasma membrane Ca²⁺ ATPase (PMCA) and Na⁺/Ca²⁺ exchangers (NCX), as well as Ryanodine receptors (RyR) on the SA membrane (see schematic in Figure 1E) were adapted and integrated into a diffusion-reaction model for cytosolic and endoplasmic Ca²⁺ dynamics (c.f., Breit et al., 2018). Numerical simulations were carried out on computational domains defined by the reconstructed human dendritic spine morphologies, using established numerical methods (details provided in Methods).

We recently showed that 70% of all dendritic spines on layer II/III pyramidal neurons contain a synaptopodin cluster, i.e., SA (Lenz et al., 2021). By carefully examining EM cross sections we also obtained evidence that large human dendritic spines contain SA organelles (Lenz et al., 2021), which is consistent with earlier work on synaptopodin clusters and spine head sizes of hippocampal neurons prepared from the rodent brain (Okubo-Suzuki et al., 2008; Vlachos et al., 2009; Yap et al., 2020). However, it has remained unclear whether, among SA containing human dendritic spines, larger spines also contain larger SAs and PSDs. Although, it has been shown that spines with SA had higher head volumes and neck diameters than spines without SA (Ofer et al., 2021).

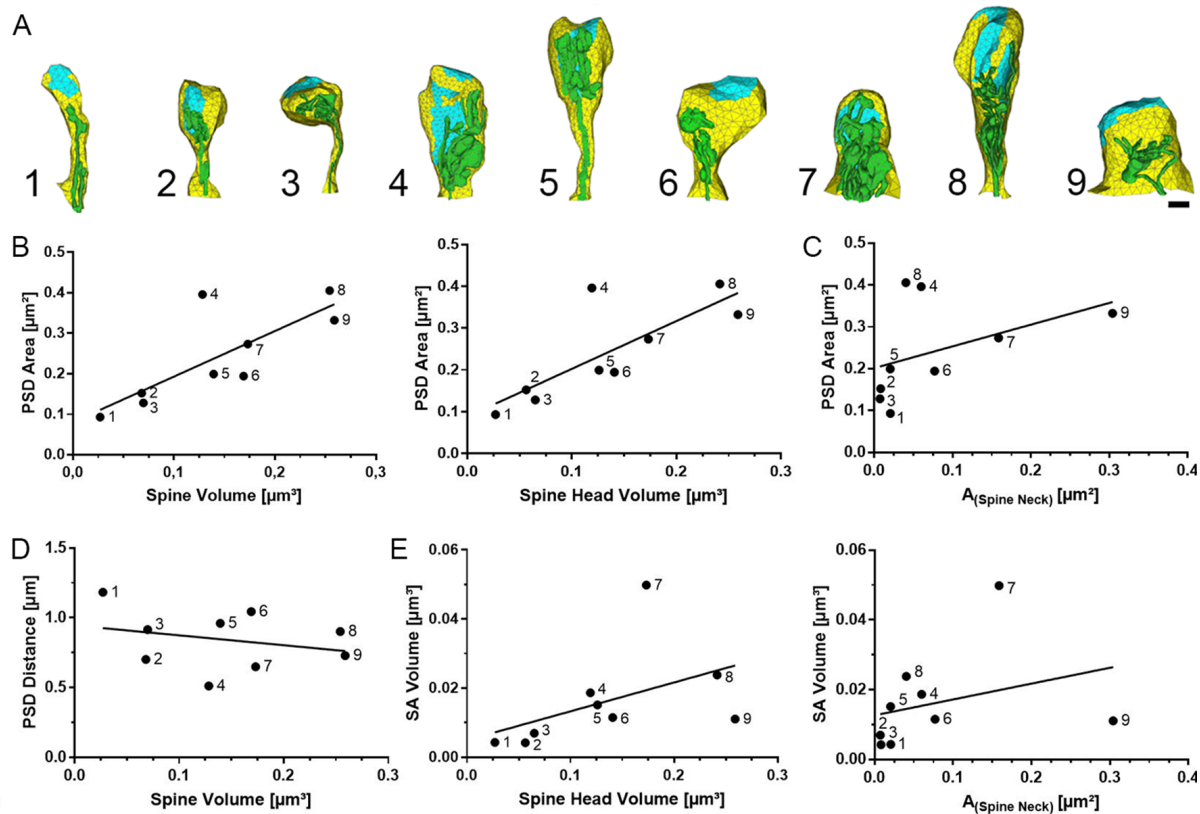


Figure 2. Morphological parameter of reconstructed spines. (A) Three-dimensional models based on reconstructed human dendritic spines. Spine apparatus organelle, green. Postsynaptic density, cyan. Scale bar, 200 nm (B) Dendritic spines with large volumes have large postsynaptic densities. (C) Positive correlation between spine neck diameter and postsynaptic density sizes (D) Postsynaptic densities in large spines are not further away from spine base. (E) Large spines contain large spine apparatus organelles, which are found in spines with wider spine necks. n = 9 reconstructed dendritic spines from 4 independent samples.

To test whether there are correlations between the reconstructed spine components, we carefully examined critical morphological parameters of the reconstructed SA-containing dendritic spines (Figure 2). Consistent with previous studies in animal models (Harris et al., 1989; Arellano et al., 2007) a positive correlation between PSD sizes and spine volumes was observed in the spines reconstructed from human cortical tissue (Figure 2A, B). This relation was readily detected when spines were sorted by spine head volumes. Moreover, a positive correlation between PSD sizes and cross-sectional area of spine necks was observed (Figure 2C). This finding raises the intriguing possibility that large spines with a wide neck may allow for a more

effective Ca²⁺ spine-to-dendrite communication. Considering the major scope of this study, i.e., modeling of spine-to-dendrite Ca²⁺ communication, we determined distances between PSDs and the dendritic compartment. Figure 2D shows no significant correlation between spine volumes and PSD-to-dendrite distances, which were defined as the Euclidian distance between the point of the PSD closest to the base of the spine. These results indicate that SA-containing spines of the human cortex may differ in their volume and spine neck diameters, while PSD-to-dendrite distances are comparable, at least for the 9 reconstructed spines used in this study.

Finally, we examined morphological properties of the SAs contained in the reconstructed spines (Figure 2E). A positive correlation was observed between spine volumes and SA volumes, which was also observed when spine neck cross-sections were considered. These results provide ultrastructural morphological insight into the three-dimensional organization of SA-containing dendritic spines in the human cortex (c.f., Lenz et al., 2021). They support the previously proposed spine-within-a-spine ER morphology, that is a critical role of spine volume and sER volume ratio in Ca²⁺ signaling (c.f., Bell et al., 2019).

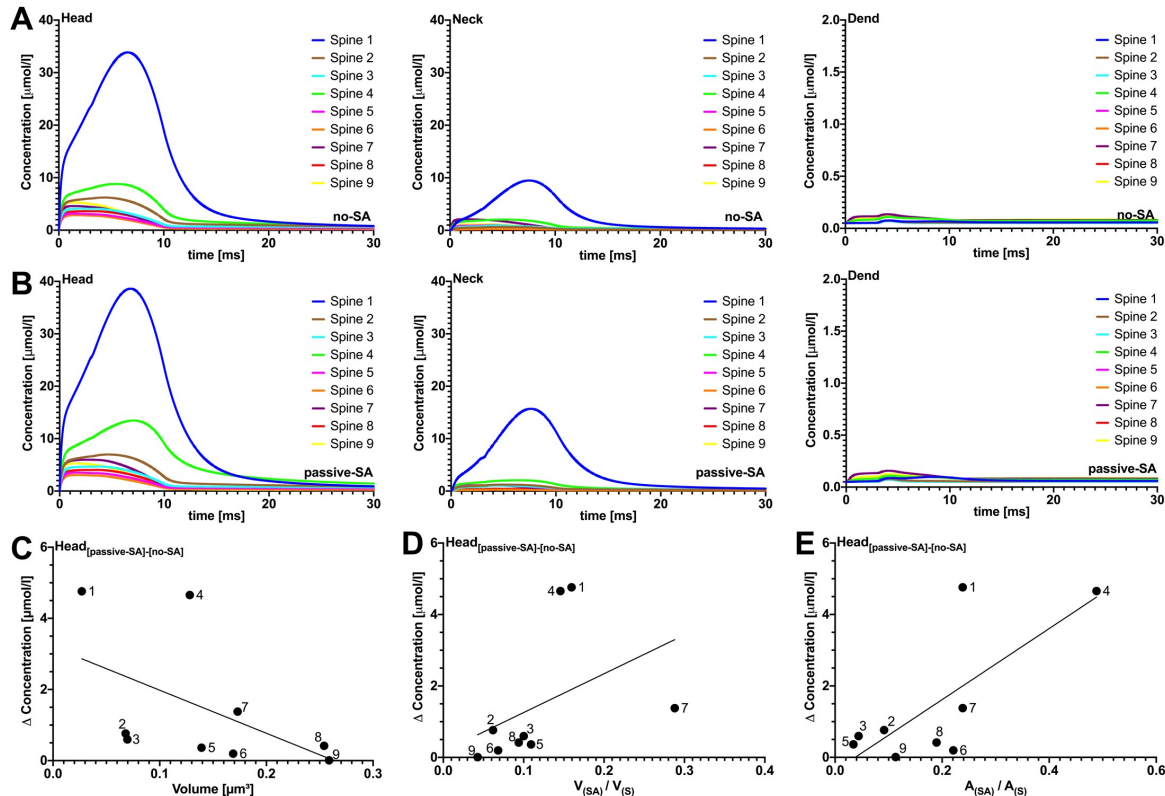


Figure 3. Effects of passive spine SA on spine-to-dendrite Ca²⁺ signaling, with fixed Ca²⁺ influx. Plots A1-A3 (without SA) and B1-B3 (with SA) show Ca²⁺ profiles for 10 ms initial Ca²⁺ release into the spine head. Consistent with experimental data, spine-to-dendrite Ca²⁺ signaling does not occur for all 9 simulated spines, and this also holds true for simulations where Ca²⁺ influx is adapted to the postsynaptic area, see additional plots. Plots C1-C3 (fixed Ca²⁺ influx) demonstrate correlations between maximum [Ca²⁺] in the head region versus spine volume, ratio of SA area/ Spine area, and SA volume/ Spine volume. Presence of a passive SA, i.e., no Ryanodine or IP₃ receptors, has no major effect on Ca²⁺ dynamics in the spine head and neck.

91 Passive SA organelles have no major impact on spine-to-dendrite Ca²⁺ signaling

To assess the role of the SA in spine-to-dendrite Ca²⁺ communication, we first investigated Ca²⁺ signal propagation in spines for which the reconstructed SA was excluded. In all simulations the same number of Ca²⁺ ions were released into the spine head at the respective PSD (Sabatini et al., 2002; Keller et al., 2008; Higley et al., 2012) and changes in [Ca²⁺] were measured in three regions of interest: the spine head, spine neck and the dendrite (Breit et al., 2018).

As shown in Figure 3A, only a small fraction of released Ca²⁺ ions reaches the dendritic compartment. To quantify the dendritic response to Ca²⁺ release at the PSD, the [Ca²⁺] amplitude was measured in the spine head, neck and dendrite. The values and ratios between head and dendrite amplitude for all spines are listed in Table 2. In all cases less than 3% of the initial [Ca²⁺] amplitude in the head was detectable in the dendrite. When the SA was added as a passive compartment, i.e., when

it was present as a geometric obstacle, but without any Ca^{2+} exchange mechanisms that would allow Ca^{2+} exchange across the SA membrane, similar and near-zero dendritic $[\text{Ca}^{2+}]$ profiles are observed in the respective spines (Figure 3B). Minor differences in the profiles (compared to the no-SA case) can be observed in the head and neck, however these all lie in the single digit $\mu\text{mol/l}$ range.

The differences in peak $[\text{Ca}^{2+}]$ amplitude between passive-SA and no-SA are presented in Figure 3C–E. These differences decrease with increasing spine volume (Figure 3C) and are positively correlated to the SA/Spine volume ratio (Figure 3D). Two clear outliers in this trend are spine 1 and 4. To test whether the SA has the ability to block calcium passage at the intersection between head and neck and thus produce larger differences in the $[\text{Ca}^{2+}]$ amplitude, the data was plotted against the SA/Spine surface area ratio at this intersection (Figure 3E). The outlier spine 4 could clearly be explained by this metric. Thus, accumulation of SA in the intersectional region between head and neck ('corking' effect) could obstruct $[\text{Ca}^{2+}]$ diffusion. Numerical simulations were also carried out for PSD adjusted Ca^{2+} influx (see Supplemental Figure 7), i.e. Ca^{2+} influx was scaled by PSD surface area, using spine 8 as the reference spine. It should be noted that PSD adjusted Ca^{2+} influx may compensate for the Ca^{2+} accumulation in the head region. In Supplemental Figure 7(C1) for instance the change in $[\text{Ca}^{2+}]$ remains relatively uniform when correlated against spine volume, with the exception of spine 4 for which we observe the above described "corking effect". Taken together, from these results (fixed Ca^{2+} and PSD adjusted) we conclude that spine-to-dendrite Ca^{2+} signaling in the dendrite is negligible for the no-SA and the passive-SA setting. These observations strengthen the case for active Ca^{2+} exchange across the spine ER membrane to enable spine-to-dendrite Ca^{2+} communication in SA containing dendritic spines.

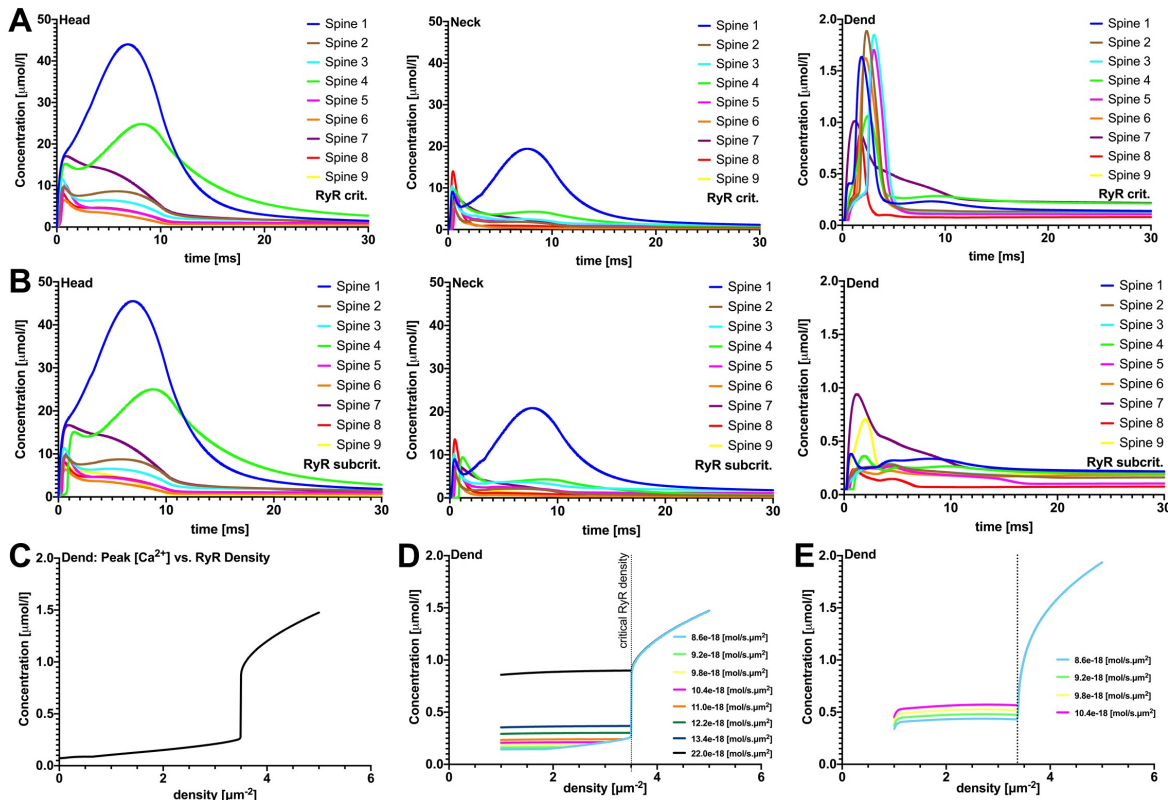


Figure 4. Effects of active SA with RyR calcium exchange mechanisms only. These plots were generated with active SA with only ryanodine receptors. For the plots in row A, these are the calcium concentration traces in the head and dendrite regions at the critical RyR density. For the plots in row B, these are the calcium concentration traces at sub-critical (5% below critical) RyR density, observe that Ca^{2+} coupling is significantly decreased. For Figures 4C-E, we demonstrate for spine 8, there is a critical RyR density such that Ca^{2+} coupling occurs in the dendritic region. The RyR density parameter is incremented at 0.01 μm^{-2} increments, observe the maximum $[\text{Ca}^{2+}]$ in the dendritic region has a significant jump at $\sim 3.50 \mu\text{m}^{-2}$. For plot D we performed the same RyR density increment experiments but with different Ca^{2+} influx at the synapse. For all spine simulations (rows A and B) we used a fixed Ca^{2+} influx at the synapse, i.e. for every spine the same calcium influx value was used.

118 **Ryanodine receptor density of SA controls spine-to-dendrite Ca²⁺ signaling**

119 Previous work revealed that RyR dependent Ca²⁺-induced Ca²⁺ release from synaptopodin associated Ca²⁺ stores modulates
120 spine Ca²⁺ dynamics and synaptic plasticity (Vlachos et al., 2009; 2013; Korkotian et al., 2014). To assess the role of active
121 SAs, by including RyRs on the membrane of the SA and dendritic ER, the RyR density critical for spine-to-dendrite Ca²⁺
122 coupling was determined for each spine (Figure 4). To quantify coupling, we defined a peak [Ca²⁺] > 1 μmol/l in the dendritic
123 measuring zone for 1 ms, with conversion this leads to 1e-18 mol/s.μm³ and multiply by the width of the dendrite (1 μm) to
124 obtain an approximate flux through the neck-dendritic interface of 1e-18 mol/s.μm², i.e., >11% of initial Ca²⁺ influx at the PSD
125 using 8.6e-18 mol/s.μm², as successful spine-to-dendrite coupling. We increased the RyR density in 0.01/μm² increments in the
126 range of 0–5 RyRs per μm² and found critical RyR values for all reconstructed morphologies, ranging between 1.37–3.5/μm²
127 (Table 1). Figure 4A shows that all spines elicit dendritic Ca²⁺ coupling when the critical RyR density is surpassed. However,
128 the peak [Ca²⁺] drops below 1 μmol/l when the RyR density is subcritical (Figure 4B). Thus, RyR density plays a critical role
129 in spine-to-dendrite coupling.

130 We next tested whether changes in calcium entry at the PSD affect the critical RyR density by successively increasing
131 the Ca²⁺ flux density at the PSD entry site. However, coupling occurs at the same RyR density, independent of the initial
132 Ca²⁺ influx within the range 8.6e-18–22.0e-18 mol/s.μm² tested here (Figure 4C–4D). This invariance can be attributed to
133 intracellular Ca²⁺ buffering, as modifications in the buffering capacity produced a shift in the critical RyR density. This was
134 observed when we ran our simulations with half the buffering capacity, Figure 4E, causing a decrease in the critical RyR density.
135 It is worth pointing out that the transition between coupling and decoupling spine-to-dendrite Ca²⁺ signals is highly nonlinear
136 (see jumps in Figure 4C–E). With control over critical RyR density appear to have the ability to control all-or-nothing Ca²⁺
137 dynamics in the parent dendrite.

138 Comparing the peak [Ca²⁺] concentrations of passive and active SA in head and dendrite (see Table 2) shows that the
139 relative differences between passive and active ER dynamics are the result of Ca²⁺-induced Ca²⁺ release through RyRs, which
140 releases additional Ca²⁺ into the cytosol. While the critical RyR density was not dependent on Ca²⁺ influx at the PSD, we
141 further studied whether the intracellular organization may play a role.

142 **Spine morphology and neck plasticity affect spine-to-dendrite Ca²⁺ signaling**

143 Critical for endoplasmic Ca²⁺ release through RyRs is sufficient [Ca²⁺] at the endoplasmic membrane (REF). Thus, an
144 intracellular organization of the SA that would support sufficient accumulation of Ca²⁺ at the spine neck (the most confined
145 part of the spine morphology) should decrease the critical RyR density. To test this hypothesis, the critical RyR density was
146 plotted against the ratio of SA in the spine-neck to spine-neck cross-sectional area (Figure 5A). We found that the area ratio
147 correlated negatively with the RyR density, demonstrating that a smaller RyR density is sufficient to induce spine-to-dendrite
148 coupling when the SA occupies larger portions of the spine neck.

149 To highlight this correlation we reference spine 4 (Figure 2A shows that the SA lies tightly at the interface of spine head
150 and neck), which produces a sharp and pronounced release of Ca²⁺ in the dendritic shaft (Figure 4C). In comparison, spine 5
151 (Figure 2A shows that the SA forms only a thin tubule from head to dendrite) produces a more gradual Ca²⁺ change, which can
152 be attributed to the absence of substantial Ca²⁺ accumulation at the SA membrane.

153 Interestingly, we observed a positive correlation between spine and SA cross-sectional area of the spine neck (Figure 5B),
154 suggesting that the SA follows dendritic spine growth and reorganizes in such a way to support spine-to-dendrite communication.
155 In fact, previous work has demonstrated that changes in spine neck diameters accompany the induction of excitatory synaptic
156 plasticity, reflected by an increase in spine head size. Specifically, spine necks are shortened and widened after long-term
157 potentiation of excitatory neurotransmission (Tønnesen et al., 2014).

158 We therefore systematically tested whether changes in spine neck diameter can affect spine-to-dendrite Ca²⁺ communication.
159 To address the role of spine neck plasticity in spine-to-dendrite Ca²⁺ communication we ran simulations by using the
160 reconstruction of spine 6 and manually widening the spine neck by 10, 20, and 40%, while keeping the RyR density and the
161 SA morphology constant (Figure 5, modified spines 6-A, 6-B, 6-C, respectively). While the Ca²⁺ dynamics in the spine head
162 remain unchanged (Figure 5C), we observed that increasing the spine neck width caused a decrease in peak Ca²⁺ near the SA
163 membrane, therefore producing insufficient Ca²⁺ release from the SA store to maintain spine-to-dendrite coupling (Figure 5D).

164 We then tested whether an increase in RyR density could balance morphology plasticity in order to maintain coupling even
165 under spine growth and reorganization. For each of the modified spines 6-A, 6-B, and 6-C we incrementally increased the RyR
166 density and observed that a critical RyR density can be determined for all spines. Naturally, this critical value increases with
167 increasing neck width, see Figure 5E (critical RyR densities for spines 6-A, 6-B, 6-C can be found in Table 1).

168 Not only could coupling be restored but, as Figure 5F shows, the dendritic calcium profiles for all adjusted spines are nearly
169 identical. This indicates that [Ca²⁺] is sensitive to changes in spine neck and SA morphology i.e. Ca²⁺ diffusion is affected by
170 spine neck and SA geometry (Svoboda, Tank, Denk; 1996). In conclusion, we observed an all-or-nothing communication switch
171 between spine head and dendrite that is controlled by an interplay between RyR density and plasticity of spine morphology.

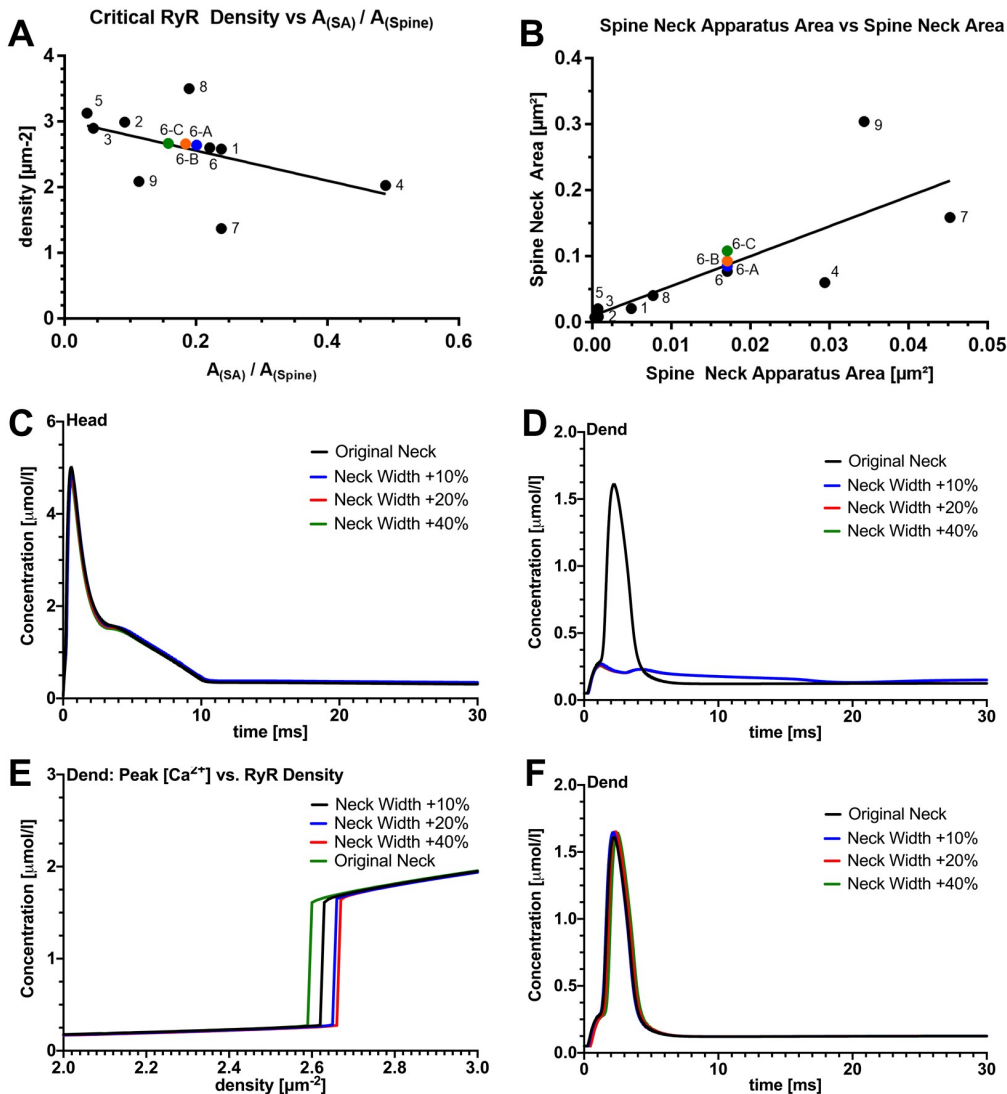


Figure 5. In figure 5.A we plot the critical RyR density agains the ratio of Spine Apparatus Neck area to Spine Neck area. In Table 1 we show the values that correspond to figure 5.A. In figures 5.C -5.D we demonstrate that widening the neck diameter of a spine affects the coupling of Ca^{2+} to the dendritic region. In particular figure 5.E indicates that neck widening causes the critical RyR density to increase.

172 Discussion

173 In this study we explored spine Ca^{2+} dynamics in human cortical spines using simulations consisting of Ca^{2+} diffusion and
 174 reaction with mobile calcium buffer (calbindin) in the cytosol, Ca^{2+} diffusion inside the SA and sER of the dendrite, as well as
 175 Ca^{2+} exchange across the plasma (PMCA, NCX) and endoplasmic (RyR) membranes (Figure 1). We show that a critical RyR
 176 density, dependent on the overall spine and SA architecture, allows active CICR release to maintain spine-to-dendrite Ca^{2+}
 177 communication. By increasing the neck diameter or decreasing the spine apparatus cross-sectional area in the neck region or
 178 individual spines this communication pathway is disrupted. Increasing the RyR density can reverse this effect (Figure 8). These
 179 findings suggest a critical role of SA- and spine neck plasticity in controlling all-or-nothing Ca^{2+} communication between the
 180 spine head and dendrite.

181 The ability to visualize individual dendritic spines in living brain tissue over extended periods was introduced three decades
 182 ago (Guthrie, Segal & Kater 1991; Müller & Connor, 1991). Consequently, the amount of information about morphology
 183 and physiology of dendritic spines and the molecular mechanisms acting on spines has tremendously increased (please cite
 184 Svoboda, Sabbatini, Holtmaat, Oertner, Sala & Segal). Yet, major issues regarding structure-function interrelations and the role
 185 of dendritic spines in network function and memory mechanisms remain unsettled (Segal 2017). This is particularly true for

186 structure-function interrelations in the adult human cortex. It is currently not possible to simultaneously visualize (1) dendritic
187 spine morphology, (2) presence and precise position of spine ER, i.e., the spine apparatus, and (3) in releasing reproducible
188 amounts of Ca²⁺ while (4) carrying out Ca²⁺ imaging at high temporal and spatial resolution in living human cortical tissue.
189 Also, it is currently impossible to systematically assess the relevance of individual spine and ER parameters, as they are not
190 easy to manipulate in biologically complex systems. To start better understanding spine Ca²⁺ dynamics in human cortical
191 neurons we employed computer simulations based on serial TEM reconstructions.

192 Our morphological analysis of the 9 reconstructed spines used in this study confirms and extends findings from a recent
193 study on synaptic plasticity of layer II/III pyramidal neurons in human cortical access material (Lenz et al., 2021). In this earlier
194 study we showed that approximately 70% of dendritic spines contain synaptopodin clusters; (2) synaptopodin clusters and
195 spine apparatus organelles are found in large dendritic spines; and (4) a plasticity-inducing stimulus promotes remodeling of
196 synaptopodin clusters, spine apparatus organelles, and dendritic spines in cortical slices prepared from the adult human brain.
197 These changes correlated well with changes in spontaneous excitatory postsynaptic currents recorded from individual layer II/III
198 pyramidal neurons. Consistent with these earlier findings, a positive correlation between SA volume, spine volumes and PSD
199 sizes is established. Likewise, we confirmed that synaptopodin is a marker for the human spine apparatus organelle (Figure
200 1X). While we have to concede that this analysis is based on 9 reconstructed spines only, disclosing such interrelation with
201 comparably small numbers indicates that these morphological measures are tightly regulated in human cortex. It likely that
202 increased use of new electron microscopy techniques such as focused ion beam, block face serial electron microscopy and array
203 tomography, together with computer based automatic 3D reconstructions will allow us to...

204 Methods

205 Ethics Statement

206 Human brain tissue was obtained from a local biobank operated in the Department for Neurosurgery at the Faculty of Medicine,
207 University of Freiburg Germany (AZ 472/15_160880). All procedures were carried out after positive evaluation by the local
208 ethics committee (AZ 593/19).

209 Electron Microscopy

210 Tissue was fixed in 4% paraformaldehyde (*w/v*) and 2% glutaraldehyde (*w/v*; phosphate buffered saline) overnight. After
211 fixation tissue was cut into 100 μm thin slices, thoroughly washed in phosphate buffer (0.1M) and incubated with 1% osmium
212 tetroxide for 60 minutes. After washing in graded ethanol (up to 50% *v/v*) for 10 minutes each, slices were incubated with
213 uranylacetat (1% (*w/v*) in 70% (*v/v*) ethanol) overnight. Slices were then dehydrated in graded ethanol (80%, 90%, 96% for
214 10 minutes each, and 2x 100% for 10 minutes). After two washing steps in propylenoxide for each 5 minutes each slice was
215 incubated with durcupan/propylenoxid (1:1 for 1 hour) following durcupan only overnight at room temperature. Ultrathin
216 sections of 20 - 40 nm were prepared at a Leica UC6 Ultracut. Sections were mounted into copper grids (Plano) and contrasted
217 using Pb-citrate for 3 minutes. Transmission electron microscopy was performed at a Zeiss Leo 906 equipped at 6000x
218 magnification. In total cortical access tissue from 7 individuals who underwent clinically indicated neurosurgical procedures,
219 e.g., for tumors or epilepsy, were processed and 1 to 6 acquisitions were obtained from each patient. Each acquisition included
220 at least one labeled dendritic segment and synaptic contact. Up to 40 images of the same dendritic spines on consecutive
221 sections were acquired and saved as TIF-files.

222 3D-reconstruction of dendritic spines and generation of spine models

223 Image series were adjusted in brightness and contrast using the Fiji software package (Schindelin et al., 2012). Stack alignment
224 and segmentation were performed with the integrated TrakEM2 plugin (Cardona et al., 2012). For this purpose, an automatic
225 alignment (rigid registration) was utilized followed by manual correction. Independent traces were drawn manually for each
226 spine attached to a dendritic segment, spine apparatus organelles and postsynaptic densities. Dendritic spines possessing spine
227 apparatus organelles that were complete within the series were reconstructed. A total of 9 series met these criteria and were
228 used in analysis. The image segmentation binary files were transformed into a preliminary surface mesh using the Java 3D
229 library (Schmid et al., 2010). However, meshes generated in this manner contained various mesh artifacts as jagged boundaries,
230 non-manifold features and surface intersection. Using the meshing software ProMesh (Reiter et al., 2013) according to a
231 post-processing scheme, conditioned surface meshes were produced which are compatible with physical simulations. Mesh
232 defects such as disconnects in the spine apparatus organelle due to thickness in ultrathin section or error in segmentation were
233 counterbalanced by manual identification and matching of cellular structures. All reconstructed spines including their spine
234 apparatus organelles were cut from their parent dendritic shaft through the base of the spine neck. Subsequently, they were
235 attached to an dendritic segment containing the endoplasmatic reticulum. Elaborating this method, we inserted realistic shapes
236 of spine apparatus into reconstructed human spine models and generated hybrids of actual anatomical morphologies with
237 simplified geometries. Using ProMesh, we directly measured volumes from the three-dimensional reconstructions. While

238 spine neck length was measured from the center of the spine head base towards the insertion of the spine to the dendrite, neck
239 diameter was calculated as an average diameter from three measurements obtained proximal, intermediate and distal to the
240 edge of the dendrite. Linear regressions were performed by best-fit approaches and were statistically tested to be different from
241 zero with the statistical software GraphPad Prism (GraphPad Software).

242 **Calcium Simulations**

243 All necessary components were implemented in the simulation toolbox NeuroBox (Breit et al., 2016). NeuroBox is a simulation
244 toolbox that combines models of electrical and biochemical signaling on one- to three-dimensional computational domains.
245 NeuroBox allows the definition of model equations, typically formulated as ordinary and partial differential equations, of the
246 cellular computational domain and specification of the mathematical discretization methods and solvers (Reiter et al., 2013;
247 Vogel et al., 2013).

248 **Model Equations**

249 **Membrane Transport Equations**

250 **Numerical Methods**

251 For numerical simulations, the four equations are discretized in space using a finite volumes method. Current densities, both
252 synaptic and across the ER and plasma membranes, can be incorporated into the reaction-diffusion process very naturally and
253 easily this way. We show how this is achieved using the cytosolic Ca²⁺ Eq. (3) as an example: It is reformulated (using the
254 divergence theorem) to an integral version

255 (integral equation)

256 where B is a control volume that will be specified shortly, and [PUT EQUATION HERE] is the outward normal on the
257 boundary of B. For control volumes located at the ER membrane, some portion of its boundary will coincide with the ER
258 membrane. Since there is no diffusive flux density [put equation here] across the ER membrane, we can simply substitute it by
259 the ER flux density j_{ERM} as given in (7) in the boundary integral for this portion of the boundary. The same applies to the
260 plasma membrane and the synapse area. Te diffusive flux is set to zero on the rest of the cytosolic domain boundary. If we
261 denote the cytosolic boundary by [A SYMBOL], its ER/plasma membrane and synaptic parts by [PUT SYMBOLS HERE],
262 respectively, this yields the following equation: (integral equation) Control volumes are constructed as a Voronoi-like dual
263 tessellation of the original tetrahedral mesh by connecting the mid-points of edges, faces and volumes through planar facets.
264 Equation (27) must hold for all control volumes, giving rise to one equation per control volume. Time discretization is realized
265 using a backwards Euler scheme, i.e., for each point in time t, the term [PUT EQUATION HERE] in (27) is replaced by the
266 discretized term [putEQUATION HERE] and all quantities on the right-hand side are evaluated at time t. Here, [PUT SYMBOL
267 HERE] is the time step size of the time discretization. By limiting the function space to the space of continuous functions that
268 are linear on all volumes of the original mesh, the integrals in Eq. (27) can be evaluated efficiently. Moreover, the solution
269 can be represented by one degree of freedom per volume, so there is one equation for each degree of freedom. The system
270 of equations arising from this procedure is nonlinear (due to the nonlinear reaction term and, more importantly, the highly
271 nonlinear transport terms across the membranes) and is therefore linearized by a Newton iteration. For the results we present
272 here, the emerging linearized problems were solved using a Bi-CGSTAB linear solver using Gauss-Seidel preconditioning.
273 Computations were facilitated by a domain decomposition parallelization approach and carried out using the UG 4 framework.

274 **References**

- 275 1. Basnayake, K. et al. Fast calcium transients in dendritic spines driven by extreme statistics. *PLOS Biol.* **17**, e2006202,
276 DOI: [10.1371/journal.pbio.2006202](https://doi.org/10.1371/journal.pbio.2006202) (2019).
- 277 2. Bell, M., Bartol, T., Sejnowski, T. & Rangamani, P. Dendritic spine geometry and spine apparatus organization govern the
278 spatiotemporal dynamics of calcium. *J. Gen. Physiol.* **151**, 1017–1034, DOI: [10.1085/jgp.201812261](https://doi.org/10.1085/jgp.201812261) (2019).
- 279 3. Berridge, M. J., Lipp, P. & Bootman, M. D. The versatility and universality of calcium signalling. *Nat. Rev. Mol. Cell Biol.*
280 **1**, 11–21, DOI: [10.1038/35036035](https://doi.org/10.1038/35036035) (2000).
- 281 4. Bloodgood, B. L., Giessel, A. J. & Sabatini, B. L. Biphasic synaptic ca influx arising from compartmentalized electrical
282 signals in dendritic spines. *PLoS Biol.* **7**, e1000190, DOI: [10.1371/journal.pbio.1000190](https://doi.org/10.1371/journal.pbio.1000190) (2009).
- 283 5. Breit, M. & Queisser, G. What is required for neuronal calcium waves? a numerical parameter study. *The J. Math. Neurosci.*
284 **8**, DOI: [10.1186/s13408-018-0064-x](https://doi.org/10.1186/s13408-018-0064-x) (2018).
- 285 6. Breit, M., Kessler, M., Stepniewski, M., Vlachos, A. & Queisser, G. Spine-to-dendrite calcium modeling discloses
286 relevance for precise positioning of ryanodine receptor-containing spine endoplasmic reticulum. *Sci. Reports* **8**, DOI:
287 DOI: [10.1038/s41598-018-33343-9](https://doi.org/10.1038/s41598-018-33343-9) (2018).

- 288 7. Cartailler, J., Kwon, T., Yuste, R. & Holcman, D. Deconvolution of voltage sensor time series and electro-diffusion
289 modeling reveal the role of spine geometry in controlling synaptic strength. *Neuron* **97**, 1126–1136.e10, DOI: [10.1016/j.neuron.2018.01.034](https://doi.org/10.1016/j.neuron.2018.01.034) (2018).
- 291 8. Deller, T. *et al.* Synaptopodin-deficient mice lack a spine apparatus and show deficits in synaptic plasticity. *Proc. Natl.
292 Acad. Sci.* **100**, 10494–10499, DOI: [10.1073/pnas.1832384100](https://doi.org/10.1073/pnas.1832384100) (2003).
- 293 9. Demmel, J., Eisenstat, S. C., Gilbert, J., Li, X. & Liu, J. A supernodal approach to sparse partial pivoting. *SIAM J. Matrix
294 Anal. Appl.* **20**, 720–755 (1999).
- 295 10. Graupner, M., Erler, F. & Meyer-Hermann, M. A theory of plasma membrane calcium pump stimulation and activity. *J.
296 Biol. Phys.* **31**, 183–206, DOI: [10.1007/s10867-005-4472-2](https://doi.org/10.1007/s10867-005-4472-2) (2005).
- 297 11. Graupner, M. *A theory of plasma membrane calcium pump function and its consequences for presynaptic calcium dynamics.*
298 Ph.D. thesis, Diploma thesis, Technische Universität Dresden (2003).
- 299 12. Higley, M. J. & Sabatini, B. L. Calcium signaling in dendrites and spines: Practical and functional considerations. *Neuron*
300 **59**, 902–913, DOI: [10.1016/j.neuron.2008.08.020](https://doi.org/10.1016/j.neuron.2008.08.020) (2008).
- 301 13. Higley, M. J. & Sabatini, B. L. Calcium signaling in dendritic spines. *Cold Spring Harb. Perspectives Biol.* **4**, a005686–
302 a005686, DOI: [10.1101/cshperspect.a005686](https://doi.org/10.1101/cshperspect.a005686) (2012).
- 303 14. Holthoff, K., Kovalchuk, Y. & Konnerth, A. Dendritic spikes and activity-dependent synaptic plasticity. *Cell Tissue Res.*
304 **326**, 369–377, DOI: [10.1007/s00441-006-0263-8](https://doi.org/10.1007/s00441-006-0263-8) (2006).
- 305 15. Jahr, C. E. & Stevens, C. F. Calcium permeability of the n-methyl-d-aspartate receptor channel in hippocampal neurons in
306 culture. *Proc. Natl. Acad. Sci.* **90**, 11573–11577, DOI: [10.1073/pnas.90.24.11573](https://doi.org/10.1073/pnas.90.24.11573) (1993).
- 307 16. Jahr, C. & Stevens, C. Voltage dependence of NMDA-activated macroscopic conductances predicted by single-channel
308 kinetics. *The J. Neurosci.* **10**, 3178–3182, DOI: [10.1523/jneurosci.10-09-03178.1990](https://doi.org/10.1523/jneurosci.10-09-03178.1990) (1990).
- 309 17. Keizer, J. & Levine, L. Ryanodine receptor adaptation and ca2+(–)induced ca2+ release-dependent ca2+ oscillations.
310 *Biophys. J.* **71**, 3477–3487, DOI: [10.1016/s0006-3495\(96\)79543-7](https://doi.org/10.1016/s0006-3495(96)79543-7) (1996).
- 311 18. Korkotian, E., Frotscher, M. & Segal, M. Synaptopodin regulates spine plasticity: Mediation by calcium stores. *J. Neurosci.*
312 **34**, 11641–11651, DOI: [10.1523/jneurosci.0381-14.2014](https://doi.org/10.1523/jneurosci.0381-14.2014) (2014).
- 313 19. Maggio, N. & Vlachos, A. Synaptic plasticity at the interface of health and disease: New insights on the role of endoplasmic
314 reticulum intracellular calcium stores. *Neuroscience* **281**, 135–146, DOI: [10.1016/j.neuroscience.2014.09.041](https://doi.org/10.1016/j.neuroscience.2014.09.041) (2014).
- 315 20. Nimchinsky, E. A. The number of glutamate receptors opened by synaptic stimulation in single hippocampal spines. *J.
316 Neurosci.* **24**, 2054–2064, DOI: [10.1523/jneurosci.5066-03.2004](https://doi.org/10.1523/jneurosci.5066-03.2004) (2004).
- 317 21. Nishiyama, J. & Yasuda, R. Biochemical computation for spine structural plasticity. *Neuron* **87**, 63–75, DOI: [10.1016/j.neuron.2015.05.043](https://doi.org/10.1016/j.neuron.2015.05.043) (2015).
- 318 22. Ofer, N., Berger, D. R., Kasthuri, N., Lichtman, J. W. & Yuste, R. Ultrastructural analysis of dendritic spine necks reveals
319 a continuum of spine morphologies. *bioRxiv* DOI: [10.1101/2021.02.18.431725](https://doi.org/10.1101/2021.02.18.431725) (2021). <https://www.biorxiv.org/content/early/2021/02/18/2021.02.18.431725.full.pdf>.
- 320 23. Padamsey, Z., Foster, W. J. & Emptage, N. J. Intracellular ca2+ release and synaptic plasticity: A tale of many stores. *The
321 Neurosci.* **25**, 208–226, DOI: [10.1177/1073858418785334](https://doi.org/10.1177/1073858418785334) (2018).
- 322 24. Perez-Alvarez, A. *et al.* Endoplasmic reticulum visits highly active spines and prevents runaway potentiation of synapses.
323 *Nat. Commun.* **11**, DOI: [10.1038/s41467-020-18889-5](https://doi.org/10.1038/s41467-020-18889-5) (2020).
- 324 25. Porter, K. R. OBSERVATIONS ON a SUBMICROSCOPIC BASOPHILIC COMPONENT OF CYTOPLASM. *J. Exp.
325 Medicine* **97**, 727–750, DOI: [10.1084/jem.97.5.727](https://doi.org/10.1084/jem.97.5.727) (1953).
- 326 26. Pozzo-Miller, L. D., Connor, J. A. & Andrews, S. B. Microheterogeneity of calcium signalling in dendrites. *The J. Physiol.*
327 **525**, 53–61, DOI: [10.1111/j.1469-7793.2000.t01-1-00053.x](https://doi.org/10.1111/j.1469-7793.2000.t01-1-00053.x) (2000).
- 328 27. Sabatini, B. L., Oertner, T. G. & Svoboda, K. The life cycle of ca2+ ions in dendritic spines. *Neuron* **33**, 439–452, DOI:
329 [10.1016/s0896-6273\(02\)00573-1](https://doi.org/10.1016/s0896-6273(02)00573-1) (2002).
- 330 28. Sala, C. & Segal, M. Dendritic spines: The locus of structural and functional plasticity. *Physiol. Rev.* **94**, 141–188, DOI:
331 [10.1152/physrev.00012.2013](https://doi.org/10.1152/physrev.00012.2013) (2014).
- 332 29. Saris, N.-E. L., Mervaala, E., Karppanen, H., Khawaja, J. A. & Lewenstam, A. Magnesium. *Clin. Chimica Acta* **294**, 1–26,
333 DOI: [10.1016/s0009-8981\(99\)00258-2](https://doi.org/10.1016/s0009-8981(99)00258-2) (2000).

- 336 30. Schmidt, H., Stiefel, K. M., Racay, P., Schwaller, B. & Eilers, J. Mutational analysis of dendritic Ca^{2+} kinetics in rodent
337 purkinje cells: role of parvalbumin and calbindin d28k. *The J. Physiol.* **551**, 13–32, DOI: [10.1113/jphysiol.2002.035824](https://doi.org/10.1113/jphysiol.2002.035824)
338 (2003).
- 339 31. Shewchuk, J. Constrained delaunay tetrahedralizations and provably good boundary recovery. In *IMR* (2002).
- 340 32. Si, H. TetGen, a delaunay-based quality tetrahedral mesh generator. *ACM Transactions on Math. Softw.* **41**, 1–36, DOI:
341 [10.1145/2629697](https://doi.org/10.1145/2629697) (2015).
- 342 33. Stepniewski, M., Breit, M., Hoffer, M. & Queisser, G. NeuroBox: computational mathematics in multiscale neuroscience.
343 *Comput. Vis. Sci.* **20**, 111–124, DOI: [10.1007/s00791-019-00314-0](https://doi.org/10.1007/s00791-019-00314-0) (2019).
- 344 34. Stutzmann, G. E. & Mattson, M. P. Endoplasmic reticulum Ca^{2+} handling in excitable cells in health and disease.
345 *Pharmacol. Rev.* **63**, 700–727, DOI: [10.1124/pr.110.003814](https://doi.org/10.1124/pr.110.003814) (2011).
- 346 35. Svoboda, K., Tank, D. W. & Denk, W. Direct measurement of coupling between dendritic spines and shafts. *Science* **272**,
347 716–719, DOI: [10.1126/science.272.5262.716](https://doi.org/10.1126/science.272.5262.716) (1996).
- 348 36. Tinker, A., Lindsay, A. R. G. & Williams, A. J. Cation conduction in the calcium release channel of the cardiac
349 sarcoplasmic reticulum under physiological and pathophysiological conditions. *Cardiovasc. Res.* **27**, 1820–1825, DOI:
350 [10.1093/cvr/27.10.1820](https://doi.org/10.1093/cvr/27.10.1820) (1993).
- 351 37. Tønnesen, J. & Nägerl, U. V. Dendritic spines as tunable regulators of synaptic signals. *Front. Psychiatry* **7**, DOI:
352 [10.3389/fpsyg.2016.00101](https://doi.org/10.3389/fpsyg.2016.00101) (2016).
- 353 38. Ulinski, P. S., Jones, E. G. & Peters, A. (eds.) *Cerebral Cortex* (Springer US, 1999).
- 354 39. van der Vorst, H. A. Bi-CGSTAB: A fast and smoothly converging variant of bi-CG for the solution of nonsymmetric
355 linear systems. *SIAM J. on Sci. Stat. Comput.* **13**, 631–644, DOI: [10.1137/0913035](https://doi.org/10.1137/0913035) (1992).
- 356 40. Verkhratsky, A. Physiology and pathophysiology of the calcium store in the endoplasmic reticulum of neurons. *Physiol.
357 Rev.* **85**, 201–279, DOI: [10.1152/physrev.00004.2004](https://doi.org/10.1152/physrev.00004.2004) (2005).
- 358 41. Vlachos, A. *et al.* Synaptopodin regulates plasticity of dendritic spines in hippocampal neurons. *J. Neurosci.* **29**, 1017–1033,
359 DOI: [10.1523/jneurosci.5528-08.2009](https://doi.org/10.1523/jneurosci.5528-08.2009) (2009).
- 360 42. Vogel, A., Reiter, S., Rupp, M., Nägel, A. & Wittum, G. UG 4: A novel flexible software system for simulating PDE based
361 models on high performance computers. *Comput. Vis. Sci.* **16**, 165–179, DOI: [10.1007/s00791-014-0232-9](https://doi.org/10.1007/s00791-014-0232-9) (2013).
- 362 43. Yap, K. *et al.* The actin-modulating protein synaptopodin mediates long-term survival of dendritic spines. *eLife* **9**, DOI:
363 [10.7554/elife.62944](https://doi.org/10.7554/elife.62944) (2020).
- 364 44. Yuste, R. & Denk, W. Dendritic spines as basic functional units of neuronal integration. *Nature* **375**, 682–684, DOI:
365 [10.1038/375682a0](https://doi.org/10.1038/375682a0) (1995).

366 **Acknowledgements**

367 We thank Sigrun Nestel for excellent technical assistance in transmission electron microscopy. This work was supported by a
368 Collaborative Research in Computational Neuroscience Grant (CRCNS; NIH and BMBF; xxxxxxxxx to GQ, 01GQ1804A to
369 AV).

370 **Tables**

Spine No.	RyR Critical Density [μm^{-2}]
1	2.58
2	2.99
3	2.9
4	2.03
5	3.13
6	2.6
6A	2.64
6B	2.66
6C	2.67
7	1.37
8	3.5
9	2.09

Table 1

Spine No.	Head - passive peak [Ca ²⁺] $\mu\text{mol/l}$	Head - active peak [Ca ²⁺] $\mu\text{mol/l}$	% Head increase	Dendrite - passive peak [Ca ²⁺] $\mu\text{mol/l}$	Dendrite - active peak [Ca ²⁺] $\mu\text{mol/l}$	% Dendrite increase
1	33.85	44	30%	0.08	1.64	1950%
2	6.22	9.66	55%	0.07	1.89	2600%
3	4.09	11.47	180%	0.07	1.85	2543%
4	8.8	24.82	180%	0.11	1.06	864%
5	3.16	10.22	223%	0.07	1.7	2329%
6	2.86	6.47	126%	0.07	1.62	2214%
7	4.6	17.09	270%	0.14	1.01	621%
8	3.62	8.11	124%	0.07	0.88	115%
9	5.29	7.2	36%	0.12	1.05	775%

Table 2

371 **Supplemental Figures**

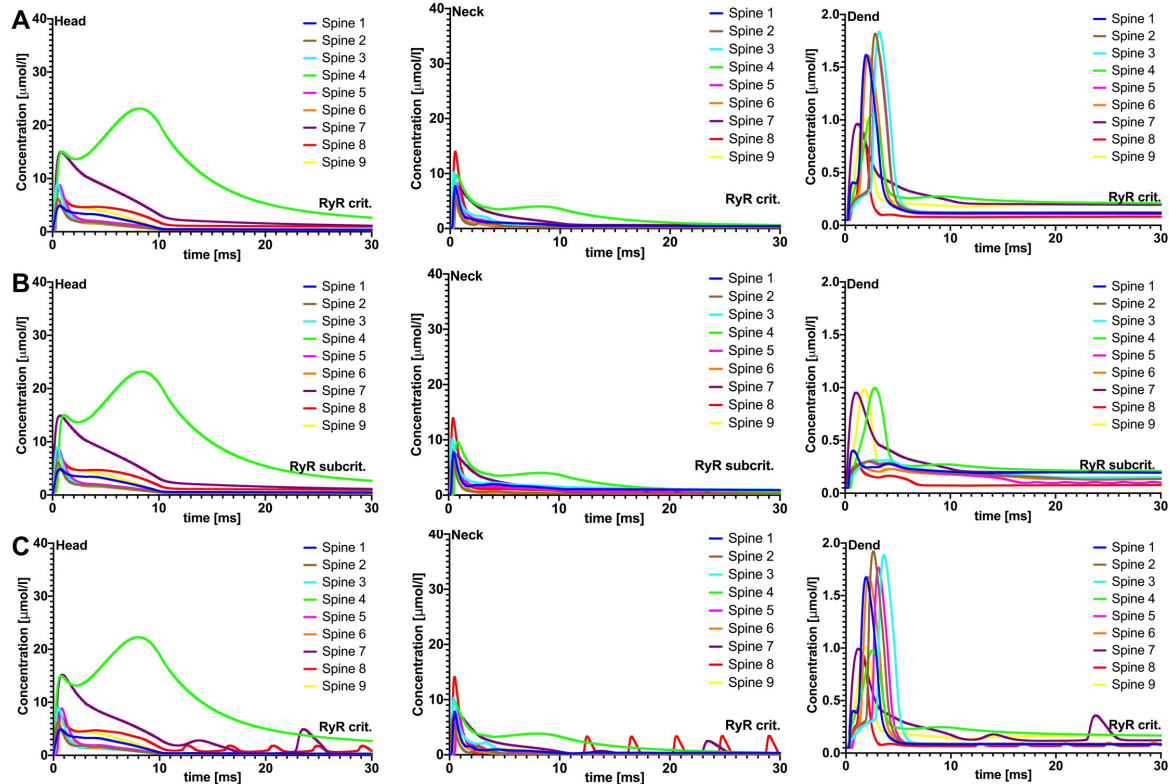


Figure 6. All plots in figure 4 were generated with PSD adjusted calcium influx. In row A, these are the calcium concentration profiles in the head and dendrite region with SERCA pumps off and at critical RyR density. In row B, these calcium concentration profiles correspond to sub-critical RyR density. In row C, these are the calcium concentration profiles at critical RyR density with SERCA pumps on. In row C, when SERCA pumps are activated we observe oscillations in the some of the calcium concentration profiles

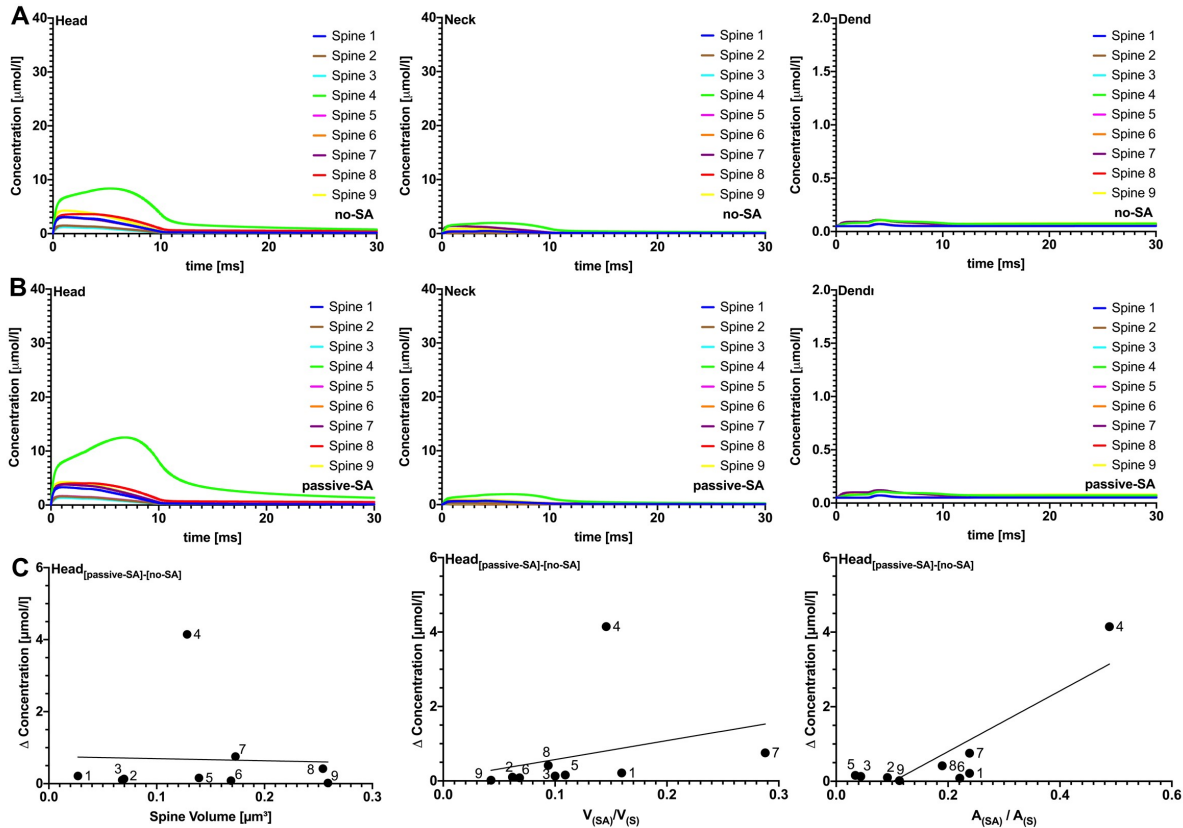


Figure 7. Figure 7: Effects of passive spine SA on spine-to-dendrite Ca²⁺ signaling, with PSD adjusted Ca²⁺ influx. Plots A1-A3 (without SA) and B1-B3 (with SA) show Ca²⁺ profiles for 10 ms initial Ca²⁺ release into the spine head. Consistent with experimental data, spine-to-dendrite Ca²⁺ signaling does not occur for all 9 simulated spines. Presence of a passive SA, i.e., no Ryanodine or IP₃ receptors, has no major effect on Ca²⁺ dynamics in the spine head and neck.